

## MAPPING SPATIALLY VARYING ADDITIVE BIASES IN COSMIC SHEAR DATA

T. D. KITCHING<sup>1,†</sup>, A. C. DESHPANDE<sup>1</sup>, P. L. TAYLOR<sup>2</sup>

<sup>1</sup>Mullard Space Science Laboratory, University College London, Holmbury St Mary, Dorking, Surrey RH5 6NT, UK

<sup>2</sup>Jet Propulsion Laboratory, California Institute of Technology, 4800 Oak Grove Drive, Pasadena, CA 91109, USA

Version October 5, 2021

### ABSTRACT

In this paper we address the challenge of extracting maps of spatially varying unknown additive biases from cosmic shear data. This is done by exploiting the isotropy of the cosmic shear field, and the anisotropy of a typical additive bias field, using an autocorrelation discrepancy map. We test this approach using simulations and find that the autocorrelation discrepancy map produces spatially varying features that are indicative of the additive bias field both in amplitude and spatial variation. We then apply this to the Dark Energy Survey Year 1 data, and find evidence for spatially varying additive biases of at most  $2 \times 10^{-3}$  on large-scales. The method can be used to empirically inform modelling of the spatially varying additive bias field in any cosmological parameter inference, and can act as a validation test for cosmic shear surveys.

### 1. INTRODUCTION

When measuring the weak lensing effect from data, biases can be introduced by several effects. These include inaccuracies in the algorithms used (Heymans et al. 2006; Massey et al. 2007; Bridle et al. 2010; Kitching et al. 2012; Mandelbaum et al. 2015), the size of the point spread function (PSF) (Hoekstra et al. 2017; Kannawadi et al. 2019; Gatti et al. 2021), detector effects (Antilogus et al. 2014), or detection effects (Hoekstra et al. 2015; Hoekstra 2021). The propagation of such biases into cosmic shear power spectra is shown in Kitching et al. (2019, 2020), that include multiplicative and additive biases and the impact of masked data sets.

In Kitching et al. (2019, 2020) it is shown that multiplicative biases only propagate into the cosmic shear power spectrum as an average (the mean taken over all observed angles on the celestial sphere), therefore they are readily accountable for via calibration of average properties with simulations, and subsequent division or multiplication of the statistics, or joint-marginalisation with cosmological parameters. However, the additive biases do not average over the celestial sphere and propagate into the observed cosmic shear power spectrum via an auto-correlation term and a cross-correlation term with the cosmic shear itself i.e. the variation of the additive bias on the celestial sphere needs to be fully accounted for; we will refer to angular variation on the celestial sphere as ‘spatial’ variation for brevity.

Treatments of additive biases to date have not fully accounted for such spatial variation. Instead biases are either assumed to be spatially constant (DES Collaboration et al. 2021; Amon et al. 2021; Joachimi et al. 2021), or propagated using an estimated auto-correlation term only (Mandelbaum et al. 2018). A more complicated treatment was presented in Hildebrandt et al. (2020) that determined a field-of-view scale spatially varying additive term and used this to correct the auto-correlation contribution to the cosmic shear correlation function.

If one had a good model for the spatial variation of the additive biases then this could then be used to account, or remove, such biases. However, the difficulty with accounting for the spatial variation of the additive term is that with an unknown bias the model to apply is by nature unknown. We note here that in general cosmic shear power spectra are insensitive to constant additive biases (due to the field being spin-2; see Kitching et al. 2019, 2020), and any random isotropic part will act as an additional shot noise term, therefore it is the anisotropic part of the additive field that is salient. In this paper we begin to address this by developing an empirical method that can extract a map of the additive bias from cosmic shear data. We compare our approach to alternatives such as smoothing the observed shear field, or determining excess expected variance.

In Section 2 we present the methodology and discuss requirements on additive biases, in Section 3 we present results of testing on simulations and an application to DES Year 1 data, and in Section 4 we discuss conclusions.

### 2. METHOD

The observed shear field, including biases, noise, and mask effects, can be written

$$\tilde{\gamma}(\mathbf{\Omega}) = W(\mathbf{\Omega})\{[1 + m_0(\mathbf{\Omega})][\gamma(\mathbf{\Omega}) + n(\mathbf{\Omega})] + m_4(\mathbf{\Omega})[\gamma^*(\mathbf{\Omega}) + n^*(\mathbf{\Omega})] + c(\mathbf{\Omega})\}, \quad (1)$$

where each of the quantities are dependent on angular coordinates  $\mathbf{\Omega} = (\theta, \phi)$ , where  $\theta$  and  $\phi$  are latitude and longitude (or R.A. and dec). We include a spin-0 mask (this nomenclature, spin- $s$  means spin positive  $s$ )  $W(\mathbf{\Omega})$  ( $W(\mathbf{\Omega}) = 1$  where data exists and  $W(\mathbf{\Omega}) = 0$  where there is no data). The true spin-2 shear is  $\gamma(\mathbf{\Omega})$ , and the measured spin-2 shear is  $\tilde{\gamma}(\mathbf{\Omega})$ .  $m_0(\mathbf{\Omega})$  and  $m_4(\mathbf{\Omega})$  are spin-0 and spin-4 position-dependent multiplicative bias terms respectively; in general each term needs to be spin-2, shear is spin-2 so at linear order only a spin-0 multiplicative bias or a spin-4 multiplied by a spin-minus 2 field can contribute.  $c(\mathbf{\Omega})$  is a spin-2 position-dependent additive bias.  $n(\mathbf{\Omega})$  is the un-lensed uncorrelated galaxy ellipticity, or the zero-lag intrinsic ellipticity field (Crittenden et al. 2001; Larsen & Challinor 2016; Blazek et al. 2015), which for a finite number of galaxies is a shot noise

<sup>†</sup>t.kitching@ucl.ac.uk, © 2021. All rights reserved.

term (Blazek et al. 2019). Any intrinsic alignment terms are captured in the  $\gamma(\mathbf{\Omega})$  term.  $*$  is a complex conjugate. In general we use  $\tilde{x}$  to mean an observed quantity.

One can take a spherical harmonic transform of the observed shear field and separate the E-mode component (that contains the cosmological information),

$$\tilde{\gamma}_{\ell m}^E = \frac{1}{2} \int d\mathbf{\Omega} [\tilde{\gamma}(\mathbf{\Omega}) {}_2Y_{\ell m}^*(\mathbf{\Omega}) + \tilde{\gamma}^*(\mathbf{\Omega}) {}_{-2}Y_{\ell m}^*(\mathbf{\Omega})] \quad (2)$$

where  $\ell$  and  $m$  are angular wavenumbers, and  ${}_sY_{\ell m}(\mathbf{\Omega})$  are spin-weighted spherical harmonics for spin- $s$ . The power spectra of the observed shear can now be determined

$$\tilde{C}_{\ell}^{EE} := \frac{1}{2\ell+1} \sum_m \tilde{\gamma}_{\ell m}^E \tilde{\gamma}_{\ell m}^{E,*} \quad (3)$$

where the sum runs over  $m = [-\ell, \ell]$ , and care must be taken disambiguate  $m$  (wavenumber) and  $m(\mathbf{\Omega})$  (position-dependent multiplicative bias).

As shown in Kitching et al. (2020) if we assume no strong coupling between the mask and the multiplicative bias fields, that terms  $\mathcal{O}(m(\mathbf{\Omega})c(\mathbf{\Omega}), m^2(\mathbf{\Omega})) = 0$ , and that the B-modes are negligible (see Kitching et al. 2019, 2020, for justification, and relaxations of, these assumptions) then the E-mode auto-correlation power spectrum is

$$\tilde{C}_{\ell}^{EE} \approx \sum_{\ell'}^L \mathcal{M}_{\ell\ell'}^{++} [(1 + 2\langle m^R(\mathbf{\Omega}) \rangle)(C_{\ell'}^{EE} + N_{\ell}) + 2C_{\ell'}^{E c_E} + C_{\ell'}^{c_E c_E}], \quad (4)$$

where  $m^R(\mathbf{\Omega}) = \mathbb{R}(m_0(\mathbf{\Omega}) + m_4(\mathbf{\Omega}))$ , and the angular brackets denote an angular average. Superscript  $c_E$  denotes a correlation of the E-mode part of the  $c(\mathbf{\Omega})$  field, superscript  $E$  denotes a correlation of the E-mode part of the  $\gamma(\mathbf{\Omega})$  field.  $N_{\ell} = \langle n_{\ell' m'} n_{\ell m}^* \rangle = \delta_{\ell\ell'}^K \delta_{mm'}^K \sigma_e^2 / N_{\text{gal}}$  is the shot noise term where  $\sigma_e^2$  is variance of the unlensed ellipticities, and  $N_{\text{gal}}$  is the effective number of galaxies (for a discussion of the effective number density see Blazek et al. 2019; Chang et al. 2013). Throughout we denote maximum  $\ell$ -mode as  $L$ , where sums over  $\ell$  run from 2 to  $L$ , and sums over  $m$  run from  $-\ell$  to  $\ell$ . The mixing matrix  $\mathcal{M}_{\ell\ell'}^{++}$  incorporates the correlation of angular modes  $\ell$  due to the mask and is defined in Kitching et al. (2020) (equation 12).

If the  $m_4(\mathbf{\Omega})$  term is small then an unbiased estimate for the shear, neglecting higher order terms  $\mathcal{O}(m(\mathbf{\Omega})c(\mathbf{\Omega}))$ , is  $\tilde{\gamma}(\mathbf{\Omega})/[1 + m_0(\mathbf{\Omega})]$  and this is the approach commonly used (e.g. DES Collaboration et al. 2021; Mandelbaum et al. 2018; Hildebrandt et al. 2020). However the treatment of the additive term is more complex. The power spectrum is insensitive to spatially constant terms, because  ${}_2Y_{\ell m}(\mathbf{\Omega}) = 0$  for  $\ell < 2$ . Furthermore, whilst on average over an ensemble of realisations of the shear field  $\langle C_{\ell}^{E c_E} \rangle = 0$  for a single realisation (as we have with data) this is non-zero, and both the terms in equation (4) must be accounted for. The change in the power spectrum caused by an additive bias is

$$\delta \tilde{C}_{\ell}^{EE} = \sum_{\ell'}^L \mathcal{M}_{\ell\ell'}^{++} [2C_{\ell'}^{E c_E} + C_{\ell'}^{c_E c_E}] = 2\tilde{C}_{\ell'}^{E c_E} + \tilde{C}_{\ell'}^{c_E c_E}. \quad (5)$$

Furthermore without a model for the  $c(\mathbf{\Omega})$  field (and hence a model for the  $c_E$  correlations) measurements of the power spectra alone cannot be used to disentangle the shear contribution from the additive bias contribution; this is fundamentally because, neglecting the multiplicative bias term, at any given  $\ell$ -mode there is one observable  $\tilde{\gamma}_{\ell m}^E$  and two unknowns  $\gamma_{\ell m}^E + c_{\ell m}^E$  that contribute. The same argument is true for EB, BE and BB contributions; however if  $\gamma^B(\mathbf{\Omega}) = 0$  then the BB power spectra can be used to determine the B-mode part of  $c(\mathbf{\Omega})$  since after correction for the noise term in such a case  $\tilde{\gamma}^B(\mathbf{\Omega}) = c^B(\mathbf{\Omega})$ . Therefore we need a way to determine the unknown E-mode component of  $c(\mathbf{\Omega})$  such that it can be removed or modelled, and this is focus of this paper.

### 2.1. Additive Requirements

Before we describe how to identify and remove additive biases it is useful to understand how requirements on additive biases propagate into the cosmic shear power spectrum. Typically biases are set either on the absolute value of the mean additive bias field components,  $|\langle c_i(\mathbf{\Omega}) \rangle| \leq R_{c_i}$ , where  $R_x$  is a requirement on  $x$ ; or on the standard deviation of the additive bias field per component  $\sigma_{c_i} \leq R_{\sigma_{c_i}}$ . Where  $R_{c_i} \simeq 10^{-4}$  and  $R_{\sigma_{c_i}} \simeq 5 \times 10^{-4}$  for a dark energy Stage-IV like experiment (Albrecht et al. 2006; Cropper et al. 2013; Massey et al. 2013). As we have commented any requirement on the mean of the additive field is nugatory because of the insensitivity of the power spectrum to constant terms. The impact of setting a requirement on  $\sigma_{c_i}$  is more complicated, but can be understood via Parseval's theorem applied to the spin-weighted spherical harmonic setting (Seibert 2018),

$$\frac{1}{4\pi} \int d\mathbf{\Omega} |f^2(\mathbf{\Omega})| = \sum_m \sum_{\ell} f_{\ell m} f_{\ell m}^* \quad \text{and} \quad \frac{1}{4\pi} \int d\mathbf{\Omega} |c_E^2(\mathbf{\Omega})| = \frac{1}{2\pi} \sigma_{c_i}^2 = \sum_{\ell} (2\ell+1) C_{\ell}^{c_E c_E}, \quad (6)$$

which we show for an arbitrary function on the sphere  $f(\mathbf{\Omega})$ , and in our case of an additive bias field, assuming that the error on each of the component of the additive field are equal. Since by definition  $C_{\ell}^{c_E c_E} > 0$  this leads to a maximum condition on the amplitude of the  $c_E c_E$  power spectrum at any given  $\ell$ -mode (corresponding to the case of a single spike at that mode) so that a

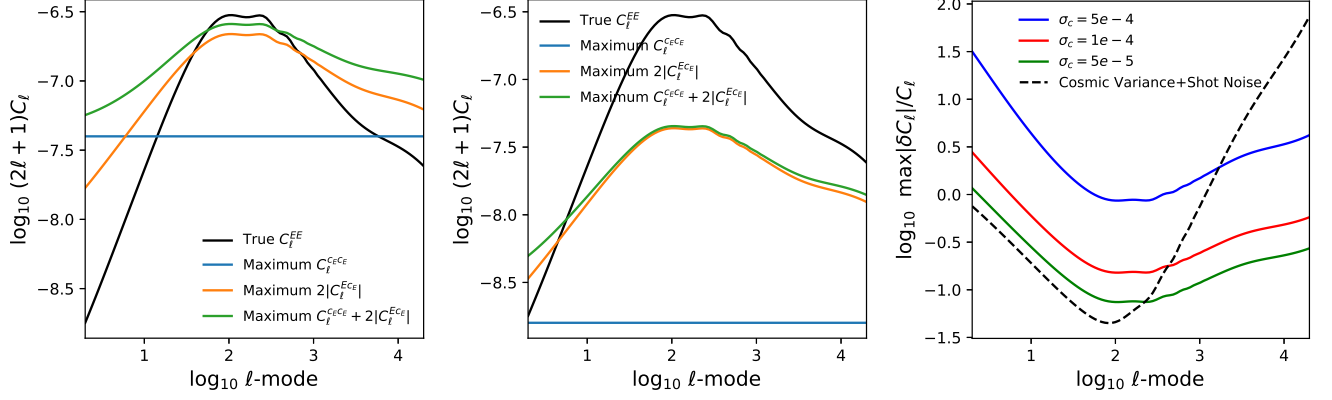


FIG. 1.— The left and middle plots show the cosmic shear power spectrum (using the set up described in Section 2), compared to the maximum imposed bounds on  $C_\ell^{cc}$  and  $C_\ell^{EE}$  by a requirement of  $\sigma_c < 5 \times 10^{-4}$  (left) and requirement of  $\sigma_c < 10^{-4}$  (middle). The right plot shows the maximum fractional allowable change on the cosmic shear power spectrum for  $\sigma_c < 5 \times 10^{-4}$  (blue) and  $\sigma_c < 10^{-4}$  (red), compared to the fractional noise contribution (cosmic variance plus shot noise) to the observed power spectrum (dashed line).

requirement  $R_{\sigma_{ci}}$  strictly leads to

$$\max[C_\ell^{EE}] \leq \frac{R_{\sigma_{ci}}^2}{[2\pi(2\ell+1)]} \quad (7)$$

for all  $\ell$ . In practice the power spectrum will not be a spike so this is very much a worst case.

Whilst the  $C_\ell^{EE} > 0$  the cross-correlation term  $C_\ell^{EE}$  can be either positive or negative. To understand the impact of a requirement on this term we can use the Cauchy-Schwarz inequality applied to complex value fields such that  $2|C_\ell^{EE}| \leq 2[C_\ell^{EE} C_\ell^{EE}]^{1/2}$  for all  $\ell$ . Given a requirement this leads to a maximum possible value of this term to be

$$\max[2|C_\ell^{EE}|] \leq 2[C_\ell^{EE}]^{1/2} \frac{R_{\sigma_{ci}}}{[2\pi(2\ell+1)]^{1/2}}. \quad (8)$$

Again in practice the auto-correlation power spectrum will not be a spike so this is very much a worst case. Therefore we find that by setting a requirement on  $R_{\sigma_{ci}}$  the amplitude of the change in the power spectrum per mode is constrained to be in a worst case

$$\max[\delta C_\ell^{EE}] \leq \max \left\{ \frac{R_{\sigma_{ci}}^2}{[2\pi(2\ell+1)]} \pm 2[C_\ell^{EE}]^{1/2} \frac{R_{\sigma_{ci}}}{[2\pi(2\ell+1)]^{1/2}} \right\} \quad (9)$$

for all  $\ell$ . Therefore in regions where  $\max[|\delta C_\ell^{EE}|]/C_\ell^{EE} \ll 1$  any residual spatially varying additive field will have a minimal impact, if the overall variance of the bias field is constrained by  $R_{\sigma_{ci}}$ . This has an interesting effect of a requirement on  $R_{\sigma_{ci}}$  being much more constraining than one may expect by also constraining the  $\ell$ -mode ranges over which one needs to be concerned.

In Figure 1 we show the maximum  $\max[C_\ell^{cc}]$ ,  $\max[2|C_\ell^{EE}|]$ , and  $\max[\delta C_\ell^{EE}]$  for  $R_{\sigma_{ci}} = 5 \times 10^{-5}$ ,  $1 \times 10^{-4}$  and  $5 \times 10^{-4}$ . It can be seen that above  $\ell \approx 1000$  the maximum changes imposed by these requirements are subdominant to the noise. The requirements suppress the maximum allowable changes at intermediate scales  $\ell \approx 100$ , but at large-scales do not.

Since already modern shape measurement methods have performances with  $\sigma_{ci} \leq 5 \times 10^{-4}$  (e.g. Hoekstra et al. 2021; Hoekstra 2021) this means we only need to be predominately concerned with the impact of additive biases for low- $\ell$  modes. Furthermore it suggests that one can set a requirement on  $\sigma_{ci}$ , without modelling a full spatially varying field and that if the requirement is small enough the impact of the spatial variation is well-constrained. These results confirm the findings of Euclid Collaboration et al. (2020) and Kitching et al. (2016) who found that for typical systematic effects constrained with a requirement on  $\sigma_{ci}$  that the power spectrum changes were predominately on large-scales. Furthermore that small-scale systematic effects were sub-dominant to the cosmic shear power spectrum and had a minimal impact on cosmological parameter inference.

## 2.2. Mapping the additive bias

To detect and remove additive biases the property that we exploit is that the shear field and the additive bias field are expected to have different generic spatial variations. The shear field is expected to be isotropic, and on large-scales close to a Gaussian random field. The additive bias field is expected to be anisotropic, and generally not a Gaussian random field; since such biases are caused by underlying processes that are not isotropic or Gaussian.

For an isotropic Gaussian field the spherical harmonic coefficients  $\gamma_{\ell m}^E$  are uncorrelated independent complex-valued variables that satisfy  $\langle \gamma_{\ell m}^E \rangle = 0$  and  $\langle \gamma_{\ell m}^E \gamma_{\ell' m'}^{E,*} \rangle = C_\ell \delta_{\ell \ell'} \delta_{mm'}^K$ . In time-series analysis departures from *iid* (independent and identically distributed random variables) distributed data can be determined via the autocorrelation (or autocovariance) function that finds significant non-*iid* behaviour by looking for excess covariance between different time steps separated by a lag (essentially the off-diagonal part of the observed time-dependent covariance matrix). In Hamann et al. (2019) this concept was generalised to spin-0 isotropic Gaussian distributed data on the sphere, and applied to Cosmic Microwave Background (CMB) data. We will

review and slightly generalise the Hamann et al. (2019) result for the case of masked cosmic shear data.

We start by considering the real part (although all the following arguments equally apply to the imaginary part) of an observed shear field that is a spin-0 field with a spherical harmonic transform

$$\tilde{\gamma}_{\ell m} = \int d\Omega [\mathbb{R}[\tilde{\gamma}(\Omega)]] {}_0Y_{\ell m}^*(\Omega), \quad (10)$$

which, similar to Hamann et al. (2019), we define for  $\ell \geq 2$  to reflect the spin-2 nature of the total shear field. We can now define the autocorrelation probe coefficients

$$\tilde{T}_\ell(\Omega) = \sum_m \tilde{\gamma}_{\ell m} {}_0Y_{\ell m}(\Omega). \quad (11)$$

If the field in question is an isotropic all-sky (unmasked) Gaussian random field then (Hamann et al. 2019)

$$\langle T_\ell(\Omega) \rangle = 0 \quad \text{and} \quad \langle T_\ell(\Omega) T_{\ell'}^*(\Omega) \rangle = \frac{(2\ell+1)}{4\pi} \tilde{C}_\ell \delta_{\ell\ell'}^K, \quad (12)$$

where angular brackets are ensemble averages and  $\langle \tilde{\gamma}_{\ell m} \tilde{\gamma}_{\ell' m'}^* \rangle = \tilde{C}_\ell \delta_{\ell\ell'}^K \delta_{mm'}^K$  is the observed power spectrum. It can also be shown that for an isotropic all-sky Gaussian random field that the variance of  $\langle T_\ell(\Omega) T_{\ell'}^*(\Omega) \rangle$  is

$$\text{var}(\langle T_\ell(\Omega) T_{\ell'}^*(\Omega) \rangle) = \frac{(2\ell+1)(2\ell'+1)}{16\pi^2} [\tilde{C}_\ell^2 \delta_{\ell\ell'}^K + \tilde{C}_\ell \tilde{C}_{\ell'}] \quad (13)$$

through use of Wick's theorem and the additive properties of the spherical harmonic functions; this agrees with Pfeifer & Deutsch (1981) who present the variance of autocorrelation estimators in the time-series case.

The central methodology is to compute the autocorrelation function  $\tilde{T}_\ell(\Omega) \tilde{T}_{\ell'}^*(\Omega)$  and to identify for each  $\Omega$  those values that exhibit an excess value with respect to the isotropic Gaussian expected values. This is done by making an *autocorrelation discrepancy map* as follows

$$\tilde{D}(\Omega) := \sum_{\ell'} \max\{|\tilde{\alpha}_{\ell'}(\Omega)| - t_{\ell'}(\Omega), 0\} \text{sgn}[\tilde{\alpha}_{\ell'}(\Omega)] \quad \text{where} \quad \tilde{\alpha}_{\ell'}(\Omega) = \sum_{\ell} |\tilde{T}_\ell(\Omega) \tilde{T}_{\ell'}^*(\Omega)| w_{\ell\ell'} \text{sgn}[\tilde{T}_\ell(\Omega)]. \quad (14)$$

$w_{\ell\ell'} = 1$  if  $0 \leq \ell' - \ell \leq k_{\max}$ , and zero otherwise, where  $k$  is referred to as the ‘lag’, and a maximum  $k_{\max}$  is chosen to optimise speed and accuracy (noting that for large lag correlations tend to be very small for most plausible additive bias fields), but in this paper we set  $k_{\max} = L$  which if computationally feasible should be done.  $\text{sgn}[x]$  is defined to be  $(-1, 0, 1)$  for  $(x < 0, x = 0, x > 1)$  respectively and is introduced to maintain the sign information of the anisotropic field.  $t_{\ell'}(\Omega)$  is a position-dependent threshold value that we define generically as the sum of the expected mean plus uncertainty

$$t_{\ell'}(\Omega) = \sum_{\ell} \langle T_\ell(\Omega) T_{\ell'}^*(\Omega) \rangle w_{\ell\ell'} + N_\sigma \left[ \sum_{\ell} \text{var}(\langle T_\ell(\Omega) T_{\ell'}^*(\Omega) \rangle w_{\ell\ell'}) \right]^{1/2} \quad (15)$$

that can be computed analytically in the all-sky case (equations 12 and 13), where  $N_\sigma$  is the number of standard deviations that a detection threshold is set. We note that the  $\tilde{\gamma}_{\ell m}$  are Gaussian distributed, and therefore so are the  $\tilde{T}_\ell(\Omega)$ , the  $\tilde{\alpha}_{\ell'}(\Omega)$  follow a normal product distribution with zero means (which can be well approximated by a Gaussian distribution for independent variables see e.g. Gaunt 2018). For an isotropic Gaussian random field the probability of  $\tilde{D}(\Omega) \neq 0$  is given by  $p(\tilde{D}(\Omega) \neq 0) \simeq k_{\max} \text{erf}[N_\sigma/2^{1/2}]$  i.e. for large  $N_\sigma$  it should be dominantly zero in the isotropic case. Any deviation away from zero is therefore a detection of a departure from the isotropic Gaussian case.

One can consider the observed field to be the sum of an isotropic and an anisotropic field  $\tilde{\gamma}_{\ell m} = \tilde{\gamma}_{\ell m}^{\text{iso}} + \tilde{\gamma}_{\ell m}^{\text{ani}}$ , and this can be substituted into equation (11) and then equation (14). The thresholding acts to eliminate the isotropic contribution for large  $N_\sigma$  – which guarantees that the probability of  $\sum_{\ell} [\sum_m \tilde{\gamma}_{\ell m}^{\text{iso}}(\Omega) {}_0Y_{\ell m}(\Omega)] [\sum_m \tilde{\gamma}_{\ell' m'}^{\text{iso}}(\Omega) {}_0Y_{\ell' m'}(\Omega)]^*$  being non-zero in the contribution to  $\tilde{D}(\Omega)$  is negligible, hence that either  $\tilde{\gamma}^{\text{iso}}(\Omega)$  and/or  $[\sum_m \tilde{\gamma}_{\ell' m'}^{\text{iso}}(\Omega) {}_0Y_{\ell' m'}(\Omega)]^*$  are negligible in the sum (this removes the  $\tilde{\gamma}_{\ell m}^{\text{iso}}$  autocorrelation and the cross correlation with  $\tilde{\gamma}_{\ell m}^{\text{ani}}$ ). Therefore in this case

$$\tilde{D}(\Omega) \simeq \sum_{\ell'} \sum_{\ell} \left( \sum_m \tilde{\gamma}_{\ell m}^{\text{ani}} {}_0Y_{\ell m}(\Omega) \right) \left( \sum_{m'} \tilde{\gamma}_{\ell' m'}^{\text{ani}} {}_0Y_{\ell' m'}(\Omega) \right)^* w_{\ell\ell'} + \text{constant} \simeq f[\tilde{\gamma}^{\text{ani}}(\Omega)]^2 + \text{constant}, \quad (16)$$

via inverse spherical harmonic transforms. The constant is equal to a sum over the variance term in equation (15), and the factor  $f = (1/[4L^2])k_{\max}(4L - 2k_{\max})$  accounts for a maximum lag being  $0 < k_{\max} \leq L$  (and therefore not covering the entire  $(\ell, \ell')$  plane); which for  $k_{\max} = L$  is  $f = 1/2$ . Therefore in the case of additive biases in cosmic shear data we find that

$$\frac{\text{sgn}[\tilde{D}(\Omega)]}{f^{1/2}} \left[ |\tilde{D}(\Omega)| - |\min[\tilde{D}(\Omega)]| \right]^{1/2} \simeq \mathbb{R}[c(\Omega)] \quad (17)$$

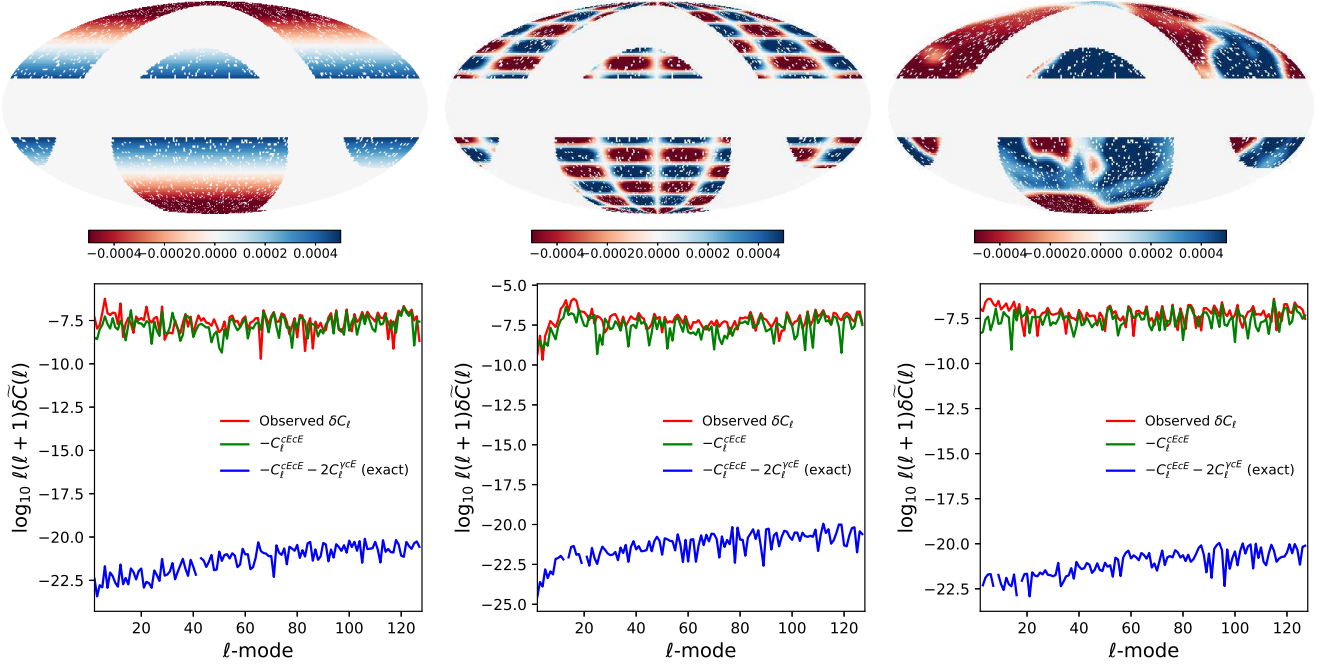


FIG. 2.— Top row: the  $c(\Omega)$  of the three masked additive bias fields used in the simulation tests, described in Section 3. Shown using a Mollweide projection. Left to right are i) a simple galactic plane; ii) a simple patch pattern; and iii) a smoothed Earth topography map. Bottom row: the change the observed EE power spectrum caused by the additive bias field. Red is the uncorrected power spectrum change; green accounts for the autocorrelation of the additive bias field, the  $C_\ell^{EE}$  term in equation (5); blue also subtracts the shear-additive field cross-correlation accounts for both terms in equation (5).

is an estimator for the real part of the additive bias field, and similarly for the imaginary part of the additive field by using  $\mathbb{I}[\tilde{\gamma}(\Omega)]$  in equation (10).

### 2.3. Masked Data

When constructing the threshold values  $t_{\ell'}(\Omega)$ , in the all-sky case the mean and variance are only dependent on the observed  $\tilde{C}_\ell$  (equations 12 and 13). However all cosmic shear data is always masked. In the case that a mask is present in the data the observed  $\tilde{\gamma}_{\ell m}$  are no longer independent and uncorrelated – only the coefficients derived from the underlying, true, shear are  $\gamma_{\ell m}$ . For a mask  $W(\Omega)$  the observed transform coefficients are related to the underlying isotropic Gaussian distributed variables via  $\tilde{\gamma}_{\ell m} = \sum_{\ell'}^L \sum_{m'} \gamma_{\ell m} W_{\ell' \ell'' mm'}$ , where  $W_{\ell' \ell'' mm'} = \int d(\Omega) {}_0Y_{\ell m}(\Omega) {}_0Y_{\ell' m'}^*(\Omega) W(\Omega)$ . This leads to an expression for  $\langle T_\ell(\Omega) T_{\ell'}^*(\Omega) \rangle$  that is dependent on the true  $C_\ell$  with a complex mode-mixing relationship

$$\langle T_\ell(\Omega) T_{\ell'}^*(\Omega) \rangle = \sum_{\ell''}^L C_{\ell''} \sum_m \sum_{m'} {}_0Y_{\ell m}(\Omega) {}_0Y_{\ell' m'}^*(\Omega) \sum_{m''} W_{\ell \ell'' mm''} W_{\ell' \ell'' m' m''} \quad (18)$$

the variance is even more complex, involving combinations of four multiplied spherical harmonic functions. In this case pursuing an analytic approach is not sensible because i) the computations are very complex/intractable in a reasonable time, ii) the computations depend on the true  $C_\ell$  not the observed  $\tilde{C}_\ell$ .

Therefore a better approach is to empirically determine the expected mean and variance of the autocorrelation functions, in order to construct the threshold values, from an ensemble of masked Gaussian random field simulations (in Appendix A we also test log-normal simulations). Therefore we follow the following approach: for a given cosmology we compute the cosmic shear power spectrum  $C_\ell$ ; we generate a set of Gaussian random field simulations  $r = \{1, \dots, N_{\text{sim}}\}$ , and for each simulation we apply the observed mask  $W(\Omega)$ ; the threshold values are computed by taking the mean and variance over the ensemble

$$t_{\ell'}(\Omega) = \text{mean}[\beta_{\ell'}(\Omega; r)] + N_\sigma \text{var}^{1/2}[\beta_{\ell'}(\Omega; r)] \quad \text{where} \quad \beta_{\ell'}(\Omega; r) = \sum_{\ell}^L [\tilde{T}_\ell(\Omega; r) \tilde{T}_{\ell'}^*(\Omega; r)] w_{\ell \ell'} \text{sgn}[\tilde{T}_\ell(\Omega; r)], \quad (19)$$

where  $T_\ell(\Omega; r)$  is for a given realisation, and the mean and variance are taken over the ensemble. This procedure leads to a set of threshold values that take into account the same mask, and associated correlations caused in the autocorrelation functions, as observed.

The final autocorrelation discrepancy map is therefore a detection of deviation from isotropy for a fixed cosmology in the masked case. In practice this should not affect the utility of the statistic since the assumed cosmology could be chosen to be that derived from the data without correcting for additive biases or a fiducial cosmology, furthermore sensitivity to the statistic to small changes in cosmology should be minimal for a sufficiently stringent threshold ( $N_\sigma \geq 3$ ).

We note that the uncertainty on the autocorrelation discrepancy map is not the  $N_\sigma$  value, which only serves as a threshold to

isolate the anisotropic signal. In the masked case the uncertainty on the autocorrelation discrepancy map is determined by the number of simulations that one can produce i.e. the threshold value itself is noisy. One can then either estimate the uncertainty via bootstrap re-sampling given a sufficiently larger number of simulations, or by creating multiple independent sets of simulations; we demonstrate this in Appendix A.

Finally we note that the approach can be iterative in that the estimate from equation (17) can be used to create a new corrected observed shear field  $\tilde{\gamma}_{i+1}(\mathbf{\Omega}) = \tilde{\gamma}(\mathbf{\Omega}) - \sum_i c_i(\mathbf{\Omega})$  where  $i$  is an iteration and the total estimate of the additive bias field over all iterations is  $\sum_i c_i(\mathbf{\Omega})$ . As  $i$  increases the residuals should tend to zero  $c_i(\mathbf{\Omega}) \rightarrow 0$ . We find in practice that this is the case even after one iteration, but we don't recommend this approach because iteration can amplify noisy parts of the estimate. Further work could extend this approach by introducing regularisation and an iterative scheme.

#### 2.4. Alternatives

Instead of the autocorrelation discrepancy map there are a few alternatives that one can try. A straightforward approach is to apply a smoothing function to the observed shear field

$$\tilde{\gamma}_{\text{smooth}}(\mathbf{\Omega}) = F[\tilde{\gamma}(\mathbf{\Omega}); \sigma_F] \quad (20)$$

where  $F$  is a filter function, that we take to be an isotropic Gaussian, and  $\sigma_F$  is the width of the Gaussian filter in radians. By applying a filter one may hope that on the scale of the filter the shear field may average to zero, leaving parts of the observed field that do not average to zero, including the additive bias field. A second alternative is to create an ensemble of realisations and create a threshold in real (angular space),  $s(\mathbf{\Omega}) = \text{mean}[\tilde{\gamma}(\mathbf{\Omega}; r)] + N_{\sigma} \text{var}^{1/2}[\tilde{\gamma}(\mathbf{\Omega}; r)]$  and determine excess values of the shear field  $\tilde{E}(\mathbf{\Omega}) := \max\{\tilde{\gamma}(\mathbf{\Omega}) - s(\mathbf{\Omega}), 0\}$ . However, this estimator is not expected to perform well since for a given position the shear field may randomly fluctuate low, or high, which may counteract the local additive field. In comparison with the autocorrelation functions at particular angular position the shear field  $\tilde{\gamma}(\mathbf{\Omega})$  does not have any unique statistical properties for an isotropic Gaussian random field, whereas  $\tilde{a}_{\ell}(\mathbf{\Omega})$  does.

### 3. RESULTS

To test the ability of the autocorrelation discrepancy maps to identify additive biases we use masked-sky simulations that include a Gaussian random field shear  $\gamma(\mathbf{\Omega})$ , an isotropic shot noise term  $n(\mathbf{\Omega})$ , and an anisotropic additive bias field  $c(\mathbf{\Omega})$ .

#### 3.1. Models

We model  $\gamma(\mathbf{\Omega})$  as a Gaussian random field using the *massmap* code (Wallis et al. 2017), assuming a DES Year 1 cosmology (Flaugher et al. 2015; Abbott et al. 2018; Morganson et al. 2018) to compute the EE cosmic shear power spectrum. The EE cosmic shear power spectrum, assuming the Limber (Limber 1953; Kitching et al. 2017; Lemos et al. 2017), flat-Universe (Taylor et al. 2018), reduced shear (Deshpande & Kitching 2020), flat-sky (Kamionkowski et al. 1998) and prefactor-unity (Kitching et al. 2017) approximations is given by:

$$C_{\ell}^{EE} = \int_0^{\chi_H} d\chi \frac{q^2(\chi)}{\chi^2} P_{\delta} \left( \frac{\ell + 1/2}{\chi}, \chi \right), \quad \text{where} \quad q(\chi) = \frac{3}{2} \Omega_M \frac{H_0^2}{c^2} \frac{\chi}{a(\chi)} \int_{\chi}^{\chi_H} d\chi' n(\chi') \frac{\chi' - \chi}{\chi}; \quad (21)$$

where  $P_{\delta}$  is the power spectrum of matter overdensities that we calculate using CAMB (Lewis et al. 2000) (we include the corrections from Mead et al. 2015, for the non-linear corrections).  $\chi$  and  $\chi_H$  are the comoving distance and comoving distance to the horizon respectively calculated using the *astropy* package (Astropy Collaboration et al. 2018, 2013),  $H_0$  is the Hubble constant,  $a$  is the scale factor of the Universe,  $\Omega_M$  is the dimensionless total matter density of the Universe, and  $c$  is the speed of light in a vacuum.  $n(\chi)$  is the galaxy distribution function of the survey, where we use the photometric DES Year 1 galaxy distribution (available at [http://desdr-server.ncsa.illinois.edu/despublic/y1a1\\_files/redshift\\_bins/](http://desdr-server.ncsa.illinois.edu/despublic/y1a1_files/redshift_bins/)) (Abbott et al. 2018).

We use a mask that removes data from less than  $20^\circ$  in both the galactic and ecliptic planes; and also 20% of pixels at random, to represent an all-sky mask with random patches removed – this gives a total observed sky fraction of  $f_{\text{sky}} = 0.4$ . The shot noise term is modelled using  $\sigma_e = 0.3$ , and  $N_{\text{gal}} = 30 f_{\text{sky}} 3600 (4\pi [180/\pi]^2)$ , which may be expected for a Stage IV experiment (Albrecht et al. 2006) with 30 galaxies per square arcminute.

For the additive bias field we investigate three different cases. The models we use are similar to those in Kitching et al. (2019, 2020): i) a simple galactic plane,  $c(\mathbf{\Omega}) = \alpha[\pi - |\phi - \pi|]$ ; ii) a simple patch pattern,  $c(\mathbf{\Omega}) = \alpha \sin(7|\phi - \pi|) \sin(7|\theta - \pi|)$ ; and iii) a Gaussian-smoothed Earth topography map (Leistedt et al. 2013) where  $c(\mathbf{\Omega}) = \alpha F(\text{Earth}(\mathbf{\Omega}); 0.05)$  projected onto the celestial sphere to represent a non-analytic function. We express these in terms of an arbitrary amplitude  $\alpha$  since these are all normalised to have a mean of zero and a variance of  $\sigma_c^2$  – this is an optimistic scenario where it is assumed there is no mean additive bias after calibration, but only a residual variance about zero. As a fiducial value we use  $\sigma_c = 5 \times 10^{-4}$ , which represents the current performance of the best shape measurement methods (e.g. Hoekstra et al. 2021; Hoekstra 2021). Throughout we use SSHT McEwen et al. (2013) to sample the sphere (McEwen & Wiaux 2011), and use a maximum  $\ell$ -mode of  $L = 128$ , and we use  $N_{\text{sim}} = 100$  (see Section 2), for the masked data case.

In Figure 2 we show the three models using  $\sigma_c = 5 \times 10^{-4}$ . We also show the change in the observed EE power spectrum caused by the additive bias, and subtract from this the autocorrelation of the additive bias field and cross-correlation of the additive bias field with the shear field. It is clear that only accounting for the autocorrelation of the additive bias field is insufficient to model the change in the power spectrum, and that the cross-correlation with the shear field must also be included, i.e. both terms in equation (5) are important.



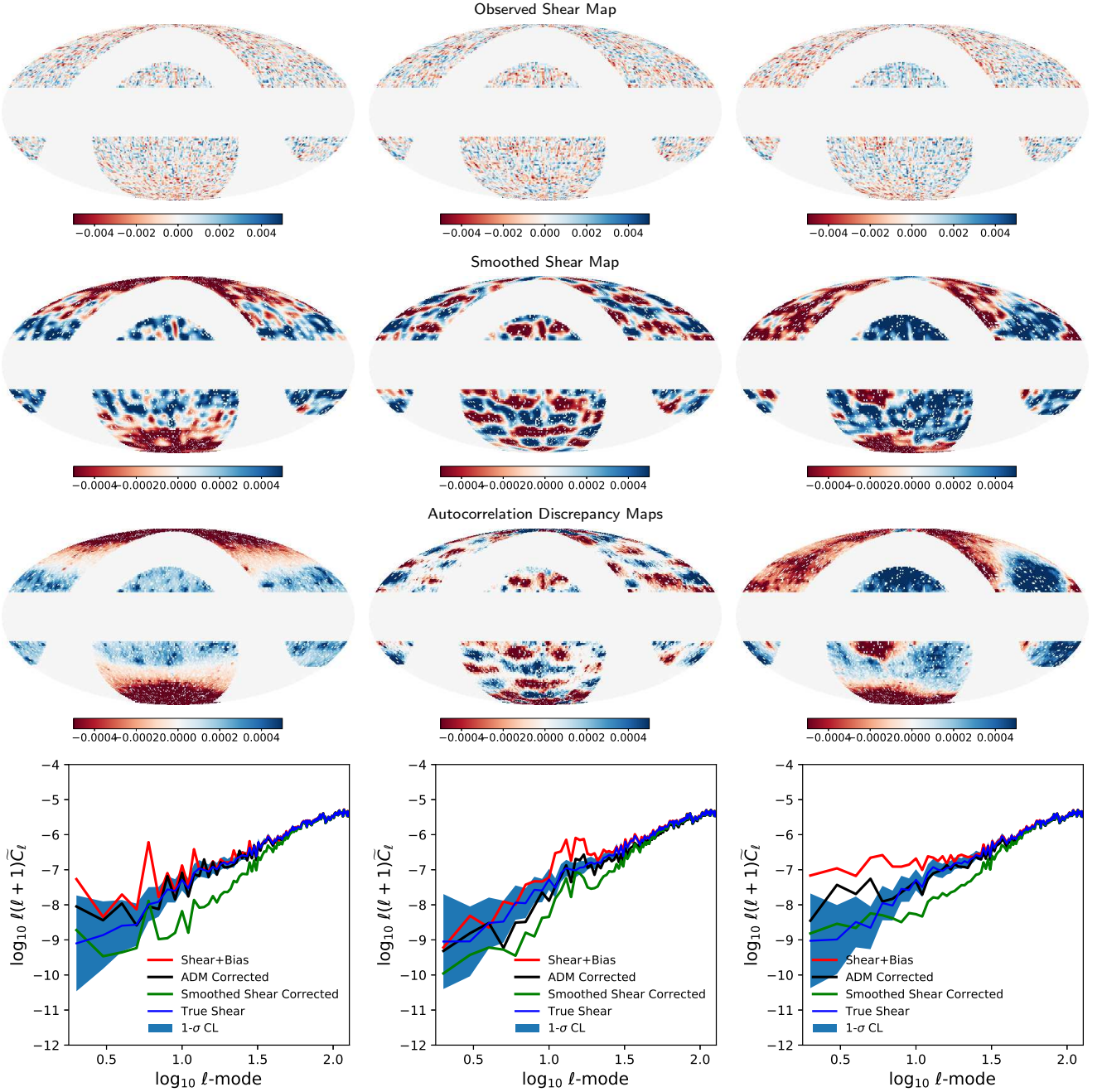


FIG. 3.— Top row: a realisation of an observed shear field, that contains the cosmic shear, shot noise and an additive bias field. Second row: the smoothed observed shear field, smoothed with a Gaussian filter of width 0.03 radians. Third row: the extracted autocorrelation discrepancy map with  $N_\sigma = 3$ . Columns left to right are for i) a simple galactic plane; ii) a simple patch pattern; and iii) a smoothed Earth topography map; which correspond to Figure 2. Bottom row: the observed shear power spectra; red includes the additive bias; black is corrected using the autocorrelation discrepancy map; green is corrected using the smoothed shear field; blue shows the true shear (without any bias) and the blue band is the  $1\sigma$  cosmic variance confidence limit.

### 3.2. Tests

In Figure 3 we show the result of testing the autocorrelation discrepancy map to extract the additive bias field from an observed shear field. For each case we show a single realisation of an observed shear field, the smoothed shear field, and the extracted autocorrelation discrepancy map. For these tests we use  $N_\sigma = 3$ . We find that in all cases the autocorrelation discrepancy map extracts a field that is indicative of the additive bias field both in amplitude and spatial variation.

We also show in the change in the observed EE power spectrum caused by the additive bias field, and the corrected power spectrum as a result of subtracting the derived additive shear field from the autocorrelation discrepancy map (equation 17) or the smoothed shear field (equation 20). We compare this with the cosmic (sample) variance about the true input shear power spectrum  $\pm 2C_\ell^{EE}/[f_{\text{sky}}(2\ell+1)]$ . We find that the autocorrelation discrepancy map results in a corrected power spectrum that is consistent with the input power spectrum. The smoothed shear correction always over-corrects the power spectrum because it removes the shear as well as the additive bias field i.e. it does not remove large-scale shear at scales larger than the smoothing

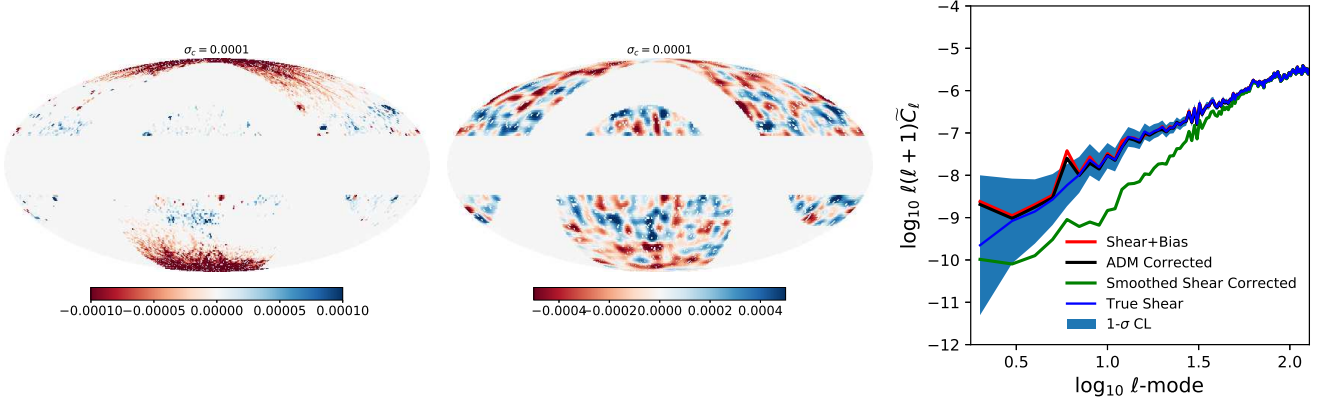


FIG. 4.— For the simple galactic plane pattern (middle rows in Figures 2 and 3) we show the autocorrelation discrepancy map for varying  $\sigma_c = 1 \times 10^{-4}, 3 \times 10^{-4}, 1 \times 10^{-3}$  (left to right), the case for  $\sigma_c = 5 \times 10^{-4}$  is the fiducial value shown in Figure 3. Note that the colour-scale varies in these plots relative to Figures 2, 3 and 8.

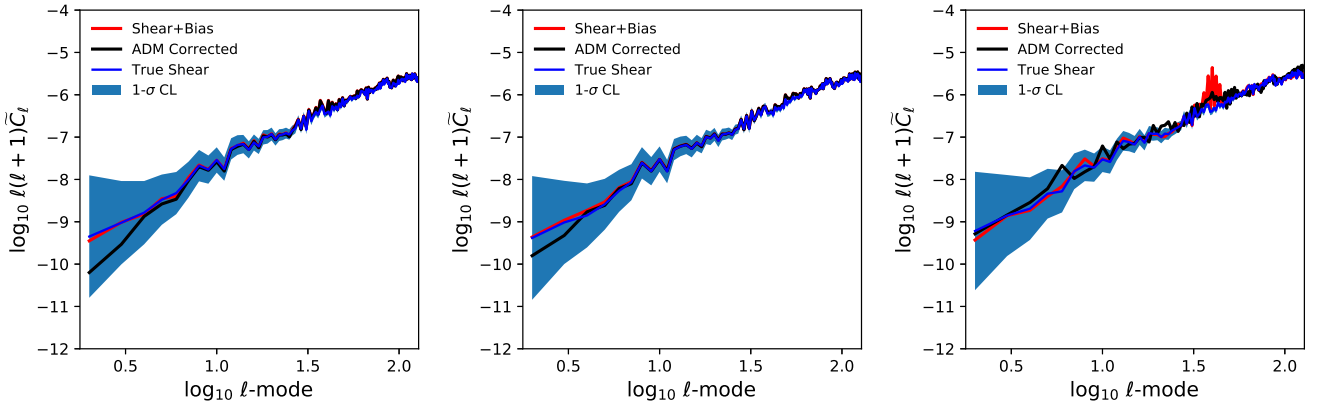


FIG. 5.— A test of the scale-dependency of the reconstructed power spectrum, for the simple pattern case. In the left and middle plots we increase the scale at which the power spectrum peaks, to  $\ell \approx 40$  and  $\ell \approx 60$ , by changing the additive bias field to  $c(\mathbf{\Omega}) = \alpha \sin(10|\phi - \pi|) \sin(10|\theta - \pi|)$  and  $c(\mathbf{\Omega}) = \alpha \sin(20|\phi - \pi|) \sin(20|\theta - \pi|)$  respectively for a fixed  $\sigma_c = 5 \times 10^{-4}$ . In the right plot we use a different pattern that is  $c(\mathbf{\Omega}) = \sum_m 2Y_{\ell_c m}(\mathbf{\Omega})$  with  $\ell_c = 40$ . In all cases the autocorrelation discrepancy map (ADM) recovers the input power spectrum.

radius of the filter.

As  $\sigma_c$  varies we will expect the performance of the autocorrelation discrepancy map to also change. But we also expect the impact of the additive bias field on the power spectrum to vary as described in Section 2.1. In Figure 4 we find for  $\sigma_c = 10^{-4}$  that the method produces an indicative map, and a power spectrum consistent with the input, but that the change in the power spectrum for this level of residual is already small, as expected.

In Figure 5 we vary the scale of the simple patch pattern such that the peak in the power occurs at smaller scales, for a fixed  $\sigma_c$ . As expected from Section 2.1 the impact of the power decreases as the scale is decreased (i.e. as the peak in the power moves to higher  $\ell$ ), and whilst the autocorrelation discrepancy map can reconstruct such features the impact on the power spectrum is negligible. We also use a different pattern that is  $c(\mathbf{\Omega}) = \sum_m 2Y_{\ell_c m}(\mathbf{\Omega})$  with  $\ell_c = 40$ , this produces a more pronounced feature, which we find is reconstructed by the autocorrelation discrepancy map.

In Appendix A we also present some further tests. The ability of the autocorrelation discrepancy map to extract the additive bias field will depend on the choice of the free parameter in the method,  $N_\sigma$ , for a given maximum multipole  $L$  and a given  $\sigma_c$ ; in Appendix A we show a test of varying this parameter. In Appendix A we also investigate the noise on the reconstructed autocorrelation discrepancy map. Finally we investigate relaxing the assumption of using Gaussian random fields, by investigating log-normally distributed shear fields.

### 3.3. Application to Data

We now test the autocorrelation discrepancy map on DES Year 1 data (Flaugher et al. 2015; Abbott et al. 2018; Morganson et al. 2018). All data products used in this Section are available here <https://doi.org/10.5281/zenodo.3980652> (first compiled in Price et al. 2021). We select galaxies with non-zero catalog weight  $w_{i,\text{DES}} > 0$  and correct for the catalogue-provided multiplicative and additive biases using

$$\tilde{\gamma}_{j,\text{DES}} = \frac{1}{N_{\text{DES}}} \sum_i^{N_{\text{gal}}} w_{i,\text{DES}} [e_{j,i,\text{DES}} - c_{j,\text{DES}}] \quad \text{where} \quad N_{\text{DES}} = \sum_i^{N_{\text{gal}}} w_{i,\text{DES}} [1 + \text{mcorr}_{j,\text{DES}}] \quad (22)$$



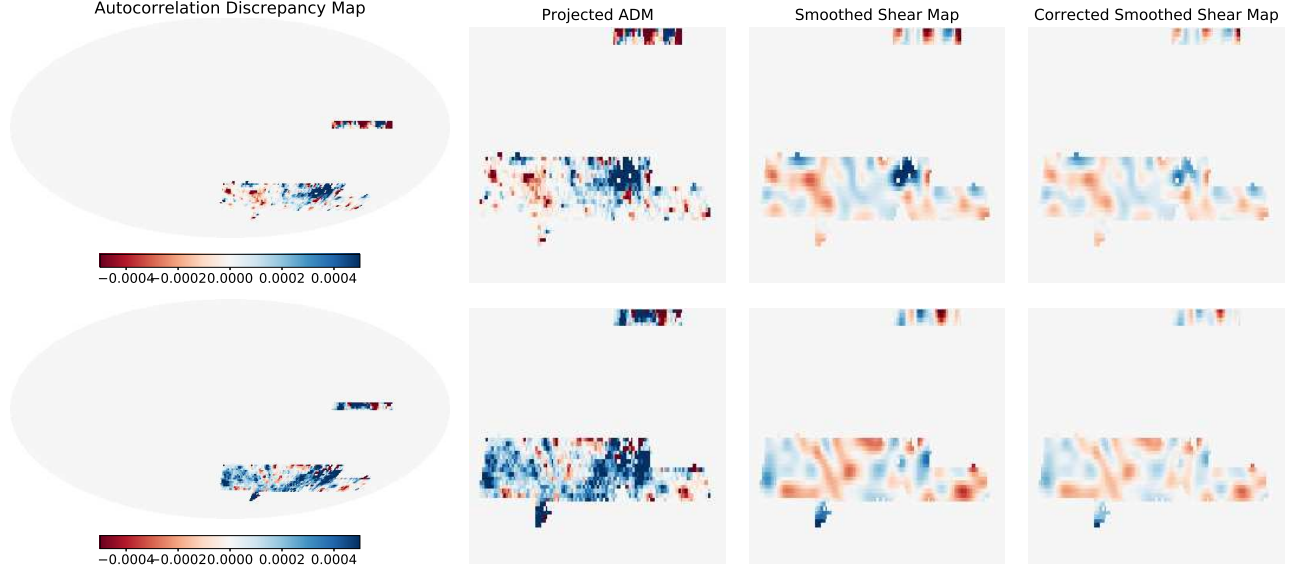


FIG. 6.— An application to DES Year 1 data. The top panels show the autocorrelation discrepancy map for the real part of the observed shear field. The left panel shows the projection on the celestial sphere with ecliptic pole at the north, the second left panel shows a planar projection of the zoomed in region where there is data, using the same colour scale as the left panel. The third left panels show the smoothed shear field, using a Gaussian filter with width 0.03 radians, using the same colour scale as the right panel. The bottom row shows the same as the top row except for the imaginary part of the observed shear field. The right panels show the smoothed shear field with the estimated additive bias removed.

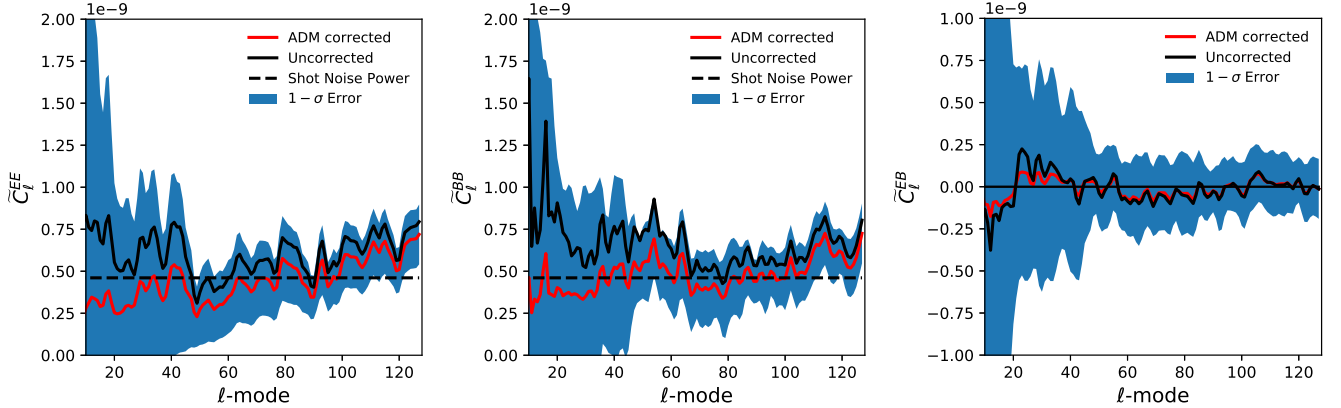


FIG. 7.— An application to DES Year 1 data. Shown are the fractional differences between the observed power spectra and the corrected power spectrum using the additive bias inferred from the autocorrelation discrepancy map (red) and smoothed shear field (green). Left to right are the EE power spectrum, the BB power spectrum and the EB power spectrum. Since the EB power spectrum is consistent with zero we only show the difference. The blue filled regions show the cosmic variance and shot noise  $1-\sigma$  confidence limits.

where  $e_{1,i,\text{DES}}$  is the DES Year 1 observed ellipticity for galaxy  $i$  for component  $j = 1, 2$ ,  $c_{j,\text{DES}}$  is the additive bias provided,  $\text{mcorr}_{j,\text{DES}}$  is the multiplicative bias correction. We use the same theoretical  $C_\ell^{EE}$  as in Section 2, which is based on the DES Year 1 cosmology, and the same  $L = 128$ . We use  $N_\sigma = 3$  and  $k_{\text{max}} = L$ .

In Figure 6 we show the autocorrelation discrepancy map for the real and imaginary parts of the shear field, and the smoothed shear field. We find evidence for spatial variation of residual biases of order  $\mathbb{R}[|c(\mathbf{\Omega})|] \simeq \mathbb{I}[|c(\mathbf{\Omega})|] \simeq 1 \times 10^{-3}$  over a large proportion of the observed field, the maximum values we find are  $\mathbb{R}[|c(\mathbf{\Omega})|] \simeq \mathbb{I}[|c(\mathbf{\Omega})|] \simeq 2 \times 10^{-3}$ . We also find some evidence for coherent spatial structure, in particular in the imaginary ( $c_2$ ) component. In comparison with the smoothed observed shear field we find similar results, albeit at lower resolution, which is consistent with our simulation test results. In Figure 7 we show the change in the observed power spectra caused by removing the estimated additive bias field, and find a  $\sim 5\%$  decrease in the observed EE and BB power spectra over the scales  $10 < \ell < 50$  (where  $\ell \sim 10$  is the fundamental mode of the survey patch in this case); the change in the EB power is consistent with zero. However, we note that at these scales the observed power spectrum is essentially consistent with noise. We note that the spatial gradient of the autocorrelation discrepancy maps is in the same direction as variations in exposure time, airmass, and sky brightness, as well as  $r$ -band depth (Drlica-Wagner et al. 2018), which warrants further investigation that we leave for future work.

#### 4. CONCLUSIONS

We present a new validation test of cosmic shear data which is the autocorrelation discrepancy map, and show that, to first order, and if multiplicative biases are removed, that the autocorrelation discrepancy map corresponds to the anisotropic part of the

absolute value of the residual additive bias field. We test this using simulations and find that the autocorrelation discrepancy map is indeed indicative of the additive bias field, and that such a map is complimentary to the approach of smoothing the observed shear field. We apply the method to DES Year 1 and find evidence for residual additive biases over the survey area of at most  $\pm 2 \times 10^{-3}$ . The method we present should be able to empirically inform the modelling of spatially additive biases which until now has relied on *a priori* modelling or proxy observables with which additive biases may be correlated. We also expect the method to perform well on galaxy clustering statistics and on CMB temperature anisotropy studies because in both cases systematic effects are in general proportional to contaminating fields, rather than the gradient of such fields as is the case in cosmic shear. It remains to be demonstrated whether this method can achieve the required accuracy for Stage-IV dark energy surveys, and a combination of template modelling (e.g. Leistedt et al. 2016) (which if the templates match the true underlying additive biases should perform well) followed by removal of any residual biases via such a method is something to explore. We present the basic method of the approach, but further work could include such statistics in more sophisticated analyses such as Bayesian Hierarchical Modelling, and a generalisation to  $3 \times 2$ -point statistics.

*Acknowledgements:* TDK acknowledges funding from the European Union’s Horizon 2020 research and innovation programme under grant agreement No 776247. ACD acknowledges funding from the Royal Society. PLT acknowledges support for this work from a NASA Postdoctoral Program Fellowship. Part of the research was carried out at the Jet Propulsion Laboratory, California Institute of Technology, under a contract with the National Aeronautics and Space Administration. We thank the developers of SSHT, `massmapy`, and `CAMB` for making their code publicly available. We thank Henk Hoekstra for helpful comments. *DES Acknowledgements:* This project used public archival data from the Dark Energy Survey (DES). Funding for the DES Projects has been provided by the U.S. Department of Energy, the U.S. National Science Foundation, the Ministry of Science and Education of Spain, the Science and Technology Facilities Council of the United Kingdom, the Higher Education Funding Council for England, the National Center for Supercomputing Applications at the University of Illinois at Urbana-Champaign, the Kavli Institute of Cosmological Physics at the University of Chicago, the Center for Cosmology and Astro-Particle Physics at the Ohio State University, the Mitchell Institute for Fundamental Physics and Astronomy at Texas A&M University, Financiadora de Estudos e Projetos, Fundação Carlos Chagas Filho de Amparo à Pesquisa do Estado do Rio de Janeiro, Conselho Nacional de Desenvolvimento Científico e Tecnológico and the Ministério da Ciência, Tecnologia e Inovação, the Deutsche Forschungsgemeinschaft, and the Collaborating Institutions in the Dark Energy Survey. The Collaborating Institutions are Argonne National Laboratory, the University of California at Santa Cruz, the University of Cambridge, Centro de Investigaciones Energéticas, Medioambientales y Tecnológicas-Madrid, the University of Chicago, University College London, the DES-Brazil Consortium, the University of Edinburgh, the Eidgenössische Technische Hochschule (ETH) Zürich, Fermi National Accelerator Laboratory, the University of Illinois at Urbana-Champaign, the Institut de Ciències de l’Espai (IEEC/CSIC), the Institut de Física d’Altes Energies, Lawrence Berkeley National Laboratory, the Ludwig-Maximilians Universität München and the associated Excellence Cluster Universe, the University of Michigan, the National Optical Astronomy Observatory, the University of Nottingham, The Ohio State University, the OzDES Membership Consortium, the University of Pennsylvania, the University of Portsmouth, SLAC National Accelerator Laboratory, Stanford University, the University of Sussex, and Texas A&M University. Based in part on observations at Cerro Tololo Inter-American Observatory, National Optical Astronomy Observatory, which is operated by the Association of Universities for Research in Astronomy (AURA) under a cooperative agreement with the National Science Foundation.

## REFERENCES

- Abbott T. M. C., et al., 2018, *ApJS*, 239, 18  
 Albrecht A., et al., 2006, arXiv e-prints, pp astro-ph/0609591  
 Amon A., et al., 2021, arXiv e-prints, p. arXiv:2105.13543  
 Antilogus P., Astier P., Doherty P., Guyonnet A., Regnault N., 2014, *Journal of Instrumentation*, 9, C03048  
 Astropy Collaboration et al., 2013, *A&A*, 558, A33  
 Astropy Collaboration et al., 2018, *AJ*, 156, 123  
 Blazek J., Vlah Z., Seljak U., 2015, *J. Cosmology Astropart. Phys.*, 2015, 015  
 Blazek J. A., MacCrann N., Troxel M. A., Fang X., 2019, *Phys. Rev. D*, 100, 103506  
 Bridle S., et al., 2010, *MNRAS*, 405, 2044  
 Chang C., et al., 2013, *MNRAS*, 434, 2121  
 Crittenden R. G., Natarajan P., Pen U.-L., Theuns T., 2001, *ApJ*, 559, 552  
 Cropper M., et al., 2013, *MNRAS*, 431, 3103  
 DES Collaboration et al., 2021, arXiv e-prints, p. arXiv:2105.13549  
 Deshpande A. C., Kitching T. D., 2020, *Phys. Rev. D*, 101, 103531  
 Drlica-Wagner A., et al., 2018, *The Astrophysical Journal Supplement Series*, 235, 33  
 Euclid Collaboration et al., 2020, *A&A*, 635, A139  
 Flaugher B., et al., 2015, *AJ*, 150, 150  
 Gatti M., et al., 2021, *MNRAS*, 504, 4312  
 Gaunt R. E., 2018, arXiv e-prints, p. arXiv:1807.03981  
 Hamann J., Le Gia Q. T., Sloan I. H., Wang Y. G., Womersley R. S., 2019, arXiv e-prints, p. arXiv:1911.11442  
 Heymans C., et al., 2006, *MNRAS*, 368, 1323  
 Hildebrandt H., et al., 2020, *A&A*, 633, A69  
 Hoekstra H., 2021, arXiv e-prints, p. arXiv:2108.10057  
 Hoekstra H., Herbonnet R., Muzzin A., Babul A., Mahdavi A., Viola M., Cacciato M., 2015, *MNRAS*, 449, 685  
 Hoekstra H., Viola M., Herbonnet R., 2017, *MNRAS*, 468, 3295  
 Hoekstra H., Kannawadi A., Kitching T. D., 2021, *A&A*, 646, A124  
 Joachimi B., et al., 2021, *A&A*, 646, A129  
 Kamionkowski M., Babul A., Cress C. M., Refregier A., 1998, *Monthly Notices of the Royal Astronomical Society*, 301, 1064  
 Kannawadi A., et al., 2019, *A&A*, 624, A92  
 Kitching T. D., et al., 2012, *MNRAS*, 423, 3163  
 Kitching T. D., Taylor A. N., Cropper M., Hoekstra H., Hood R. K. E., Massey R., Niemi S., 2016, *MNRAS*, 455, 3319  
 Kitching T. D., Alsing J., Heavens A. F., Jimenez R., McEwen J. D., Verde L., 2017, *MNRAS*, 469, 2737  
 Kitching T. D., Paykari P., Hoekstra H., Cropper M., 2019, *The Open Journal of Astrophysics*, 2, 5  
 Kitching T. D., Deshpande A. C., Taylor P. L., 2020, *The Open Journal of Astrophysics*, 3, 14  
 Larsen P., Challinor A., 2016, *MNRAS*, 461, 4343  
 Leistedt B., McEwen J. D., Vanderghaynst P., Wiaux Y., 2013, *A&A*, 558, A128  
 Leistedt B., et al., 2016, *ApJS*, 226, 24  
 Lemos P., Challinor A., Efstathiou G., 2017, *J. Cosmology Astropart. Phys.*, 2017, 014  
 Lewis A., Challinor A., Lasenby A., 2000, *ApJ*, 538, 473  
 Limber D. N., 1953, *ApJ*, 117, 134  
 Mandelbaum R., et al., 2015, *MNRAS*, 450, 2963  
 Mandelbaum R., et al., 2018, *PASJ*, 70, S25  
 Massey R., et al., 2007, *MNRAS*, 376, 13  
 Massey R., et al., 2013, *MNRAS*, 429, 661  
 McEwen J. D., Wiaux Y., 2011, *IEEE Transactions on Signal Processing*, 59, 5876  
 McEwen J. D., Puy G., Thiran J.-P., Vanderghaynst P., Van De Ville D., Wiaux Y., 2013, *IEEE Transactions on Image Processing*, 22, 2275  
 Mead A. J., Peacock J. A., Heymans C., Joudaki S., Heavens A. F., 2015, *MNRAS*, 454, 1958  
 Morganson E., et al., 2018, *PASP*, 130, 074501  
 Pfeifer P. E., Deutsch S. J., 1981, *Journal of the Royal Statistical Society. Series B (Methodological)*, 43, 28  
 Price M. A., McEwen J. D., Pratley L., Kitching T. D., 2021, *MNRAS*, 500, 5436  
 Seibert K., 2018, *Spin-weighted Spherical Harmonics and Their Application for the Construction of Tensor Slepian Functions on the Spherical Cap*. Universitätsbibliothek der Universität Siegen, <https://books.google.co.uk/books?id=DsmpwgEACAAJ>  
 Taylor A., Joachimi B., Kitching T., 2013, *MNRAS*, 432, 1928  
 Taylor P. L., Kitching T. D., McEwen J. D., Tram T., 2018, *Phys. Rev. D*, 98, 023522  
 Taylor P. L., Kitching T. D., Alsing J., Wandelt B. D., Feeney S. M., McEwen J. D., 2019, *Phys. Rev. D*, 100, 023519

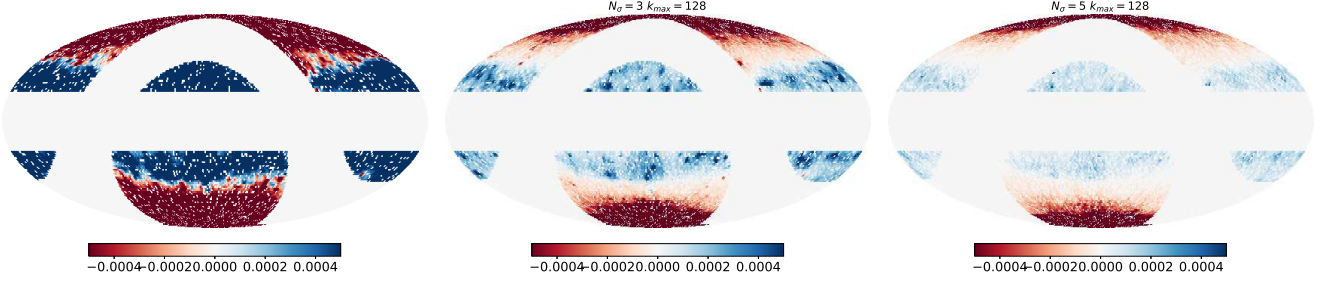


FIG. 8.— For the simple galactic plane pattern we show the autocorrelation discrepancy map for varying  $N_\sigma = 1, 3, 5$  (left to right).

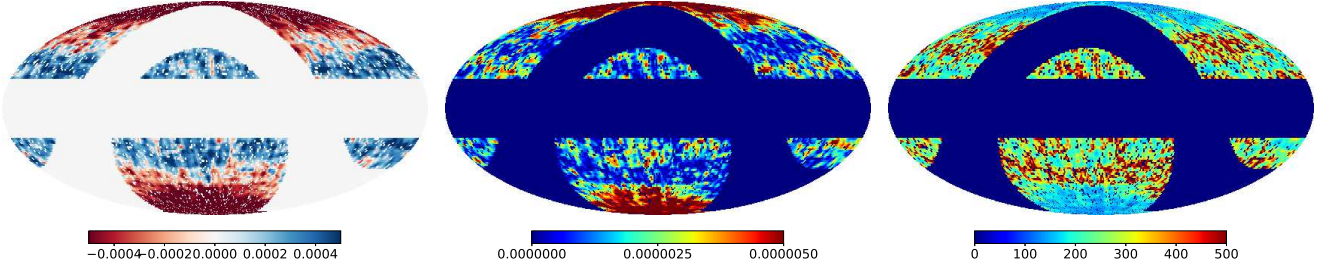


FIG. 9.— A test of the error on an autocorrelation discrepancy map. The left panel shows the mean over 100 groups of  $N_{\text{sim}} = 100$  realisations, and the middle panel shows the standard deviation over the 100 groups representing the estimate of the error on a single realisation, and the right panel shows the signal to noise (mean divided by standard deviation). We alter the colour in the middle and right panels relative to the other plots in this paper for clarity.

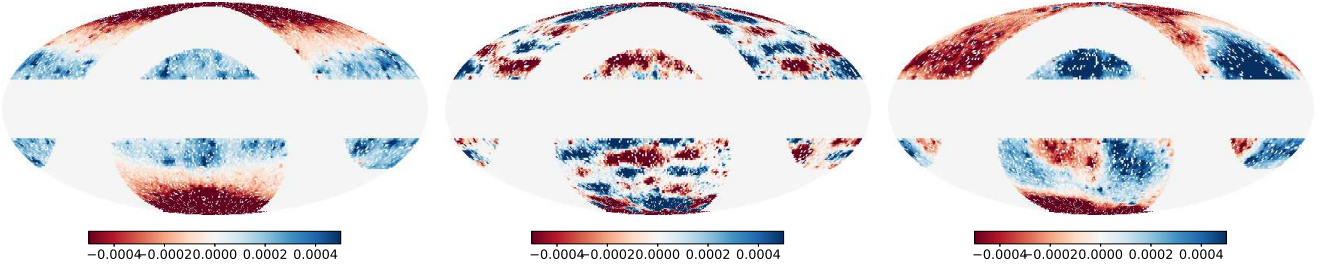


FIG. 10.— A re-analysis of the results shown in Figure 3 except using log-normal random shear fields instead of Gaussian random shear fields.

Wallis C. G. R., McEwen J. D., Kitching T. D., Leistedt B., Plouviez A.,  
2017, preprint, (arXiv:1703.09233)

#### APPENDIX A: FURTHER TESTS

In this Appendix we show some further tests of the autocorrelation discrepancy map statistic.

##### *Sensitivity*

The autocorrelation discrepancy map method has  $N_\sigma$  as a free parameter, for a given maximum multipole  $L$  and  $k_{\text{max}} = L$ . We investigate this for the simple galactic plane case in Figure 8. For  $N_\sigma$  we find a too-small value leads to noisy recovery since the isotropic part of the observed field is included in the map, and with too-large a value the probability of including a fluctuation in the statistic decreases. Therefore  $N_\sigma \approx 3$  seems approximately optimal. In practice this free parameter could be marginalised over in a likelihood analysis.

##### *Signal-to-noise*

To test the uncertainty associated with the autocorrelation discrepancy map we generate 100 groups of  $N_{\text{sim}} = 100$  realisations, using the simple galactic plane case (with  $k_{\text{max}} = 128$  and  $\sigma_c = 5 \times 10^{-4}$ ), and compute the mean and the standard deviation over the groups. In Figure 9 we show the mean over the groups and the standard deviation over the groups; noting that with only 100 groups of simulations the error on the error is approximately 10% (Taylor et al. 2013). We find that the mean error on any given realisation is approximately  $7 \times 10^{-6}$ , which is an equivalent mean signal-to-noise of approximately 120. A typical realisation can be found in Figure 3. As  $N_{\text{sim}}$  increases this would improve still further.

##### *Log-normal fields*

The autocorrelation discrepancy map statistic presented in this paper relies on statistics that depend on deviations in variance of the spherical harmonic coefficients. For a Gaussian random field these statistics are analytic and well-defined (equations 12 and 13), and we generalise to the masked case through simulations. If the spherical harmonic coefficients were not Gaussian distributed then higher-order moments of their distribution may affect the statistic. This however should not be a problem, because the spherical harmonic coefficients are created through summing over the shear field (equation 2) hence even for non-Gaussian fields the central limit theorem should result in Gaussian distributed spherical harmonic coefficients (and empirically this is found to be

the case e.g. Taylor et al. 2019). We test this by generating log-normal fields, instead of Gaussian random fields, by exponentiating the Gaussian-distributed shear field in our tests  $\gamma(\mathbf{\Omega}) \rightarrow \exp[-\gamma(\mathbf{\Omega})] - \lambda$  (where  $\lambda$  ensures the mean of the exponentiated field is zero), and re-analysing the ability of the autocorrelation correlation discrepancy to extract the additive bias field. We show the results in Figure 10 and find no change in the reconstructed maps.